

SARS-CoV-2 ORF3a expression in brain disrupts the autophagy–lysosomal pathway, impairs sphingolipid homeostasis, and drives neuropathogenesis

Hongling Zhu¹ | Colleen Byrnes¹ | Y. Terry Lee¹ | Galina Tuymetova¹ |
 Hannah B. D. Duffy¹ | Jenna Y. Bakir¹ | Sydney N. Pettit¹ | Jabili Angina¹ |
 Danielle A. Springer² | Maria L. Allende¹ | Mari Kono¹ | Richard L. Proia¹

¹Genetics of Development and Disease Section, Genetics and Biochemistry Branch, National Institute of Diabetes and Digestive and Kidney Diseases, Bethesda, Maryland, USA

²Murine Phenotyping Core, National Heart, Lung, and Blood Institute, National Institutes of Health, Bethesda, Maryland, USA

Correspondence

Richard L. Proia, Genetics of Development and Disease Section, Genetics and Biochemistry Branch, National Institute of Diabetes and Digestive and Kidney Diseases, Building 10, Room 9D-06, 10 Center DR MSC 1821, Bethesda, MD 20892-1821, USA.
 Email: proia@nih.gov

Funding information

HHS | NIH | NIDDK Division of Intramural Research (DIR); HHS | NIH | NHLBI | NHLBI Division of Intramural Research (DIR)

Abstract

Severe acute respiratory syndrome coronavirus 2 (SARS-CoV-2) infection causes injury to multiple organ systems, including the brain. SARS-CoV-2's neuropathological mechanisms may include systemic inflammation and hypoxia, as well as direct cell damage resulting from viral infections of neurons and glia. How the virus directly causes injury to brain cells, acutely and over the long term, is not well understood. In order to gain insight into this process, we studied the neuropathological effects of open reading frame 3a (ORF3a), a SARS-CoV-2 accessory protein that is a key pathological factor of the virus. Forced ORF3a brain expression in mice caused the rapid onset of neurological impairment, neurodegeneration, and neuroinflammation—key neuropathological features found in coronavirus disease (COVID-19, which is caused by SARS-CoV-2 infection). Furthermore, ORF3a expression blocked autophagy progression in the brain and caused the neuronal accumulation of α -synuclein and glycosphingolipids, all of which are linked to neurodegenerative disease. Studies with ORF3-expressing HeLa cells confirmed that ORF3a disrupted the autophagy–lysosomal pathway and blocked glycosphingolipid degradation, resulting in their accumulation. These findings indicate that, in the event of neuroinvasion by SARS-CoV-2, ORF3a expression in brain cells may drive neuropathogenesis and be an important mediator of both short- and long-term neurological manifestations of COVID-19.

1 | INTRODUCTION

Coronavirus disease 2019 (COVID-19), which is caused by the severe acute respiratory syndrome coronavirus 2 (SARS-CoV-2), can result in the damage of several organ systems, including the brain. Nervous system manifestations

commonly include loss of sense of smell, headache, and dizziness.^{1–3} More rarely, very severe neurological manifestations, such as stroke and seizure, are exhibited. A “long COVID-19” or post-COVID-19 condition that can last weeks or months after infection, in which persistent cognitive impairment is a relatively common symptom, has been

This is an open access article under the terms of the [Creative Commons Attribution License](#), which permits use, distribution and reproduction in any medium, provided the original work is properly cited.

Published 2023. This article is a U.S. Government work and is in the public domain in the USA. *The FASEB Journal* published by Wiley Periodicals LLC on behalf of Federation of American Societies for Experimental Biology.

identified.⁴ Increased risk and exacerbation of neurodegenerative disease are also emerging as possible outcomes of COVID-19.^{1,5,6} The long-term neurological manifestations of COVID-19 represent a major health concern given the magnitude of the global pandemic.

Key features of brain pathogenesis associated with COVID-19 are neuroinflammation with glial cell activation and inflammatory cytokine expression, as well as neuronal cell loss.^{7,8} COVID-19 neuropathogenesis may be caused by indirect and direct mechanisms. Indirect mechanisms include systemic inflammation, endothelial-cell damage, and hypoxia.^{3,4} Direct mechanisms, through the infection of neurons and glia by SARS-CoV-2, may be caused by cellular injury resulting from the expression of viral genes.^{4,9,10}

SARS-CoV-2 has the capacity to invade the brain,^{7,9–12} as indicated by the viral RNA and proteins that have been detected in the brains of some patients who succumbed from COVID-19, as well as from studies with nonhuman primates. Likely routes of entry are direct passage through the blood-brain barrier or via an olfactory route through the neural-mucosal interface followed by transport along the olfactory tract of the brain.¹³ Both neurons and glia are permissive for infection by the virus.^{10,14,15} However, how SARS-CoV-2 causes acute and long-term damage after direct brain cell infection is not well understood.

Virally encoded open reading frame 3a (ORF3a) is an accessory protein of SARS-CoV-2 that contributes to viral pathogenesis, disease progression, and severity of COVID-19.^{16–18} During the viral life cycle, ORF3a promotes viral release through the lysosomal exocytosis pathway and interferes with the cellular antiviral autophagy pathway, thereby suppressing intracellular viral clearance.^{19,20} By triggering cell-death pathways and pro-inflammatory responses, ORF3a may directly contribute to COVID-19 pathogenesis.^{21–23}

Because ORF3a has been identified as a potential pathogenic factor for SARS-CoV-2,^{17,18} we sought to determine the consequences of ORF3a expression in brain, which would occur in the event of viral neuroinvasion. We used an adeno-associated virus (AAV) delivery method

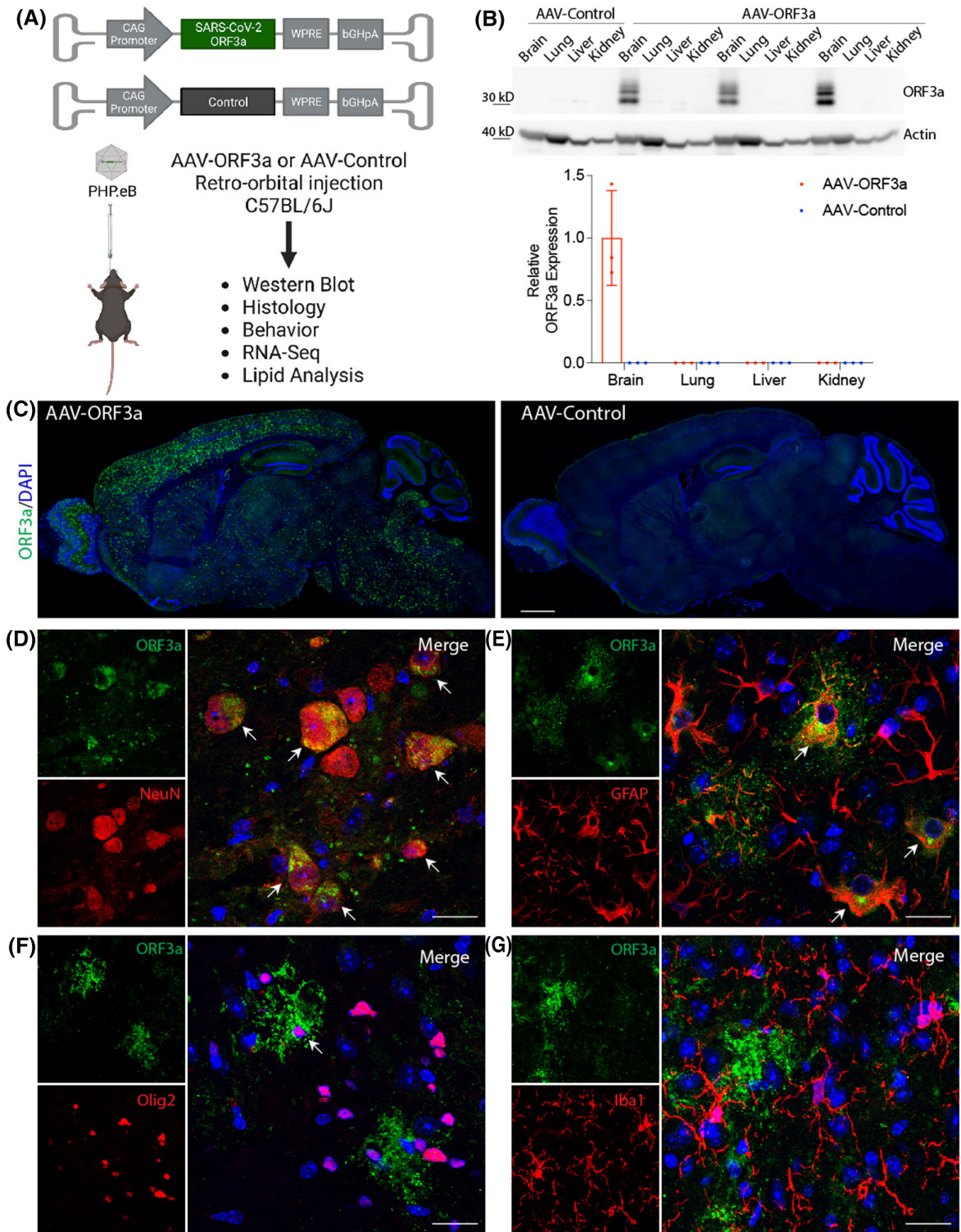
to produce selective, widespread expression of ORF3a in the brain of mice. We found that ORF3a expression rapidly induced neurological disturbances and neurodegeneration, as well as upregulation of inflammatory genes and cell death. We also found that ORF3a disrupted the autophagy-lysosomal pathway in brain and caused neuronal accumulation of α -synuclein and glycosphingolipids, factors that may be associated with neurodegenerative disease.^{24–27} These findings support an important role for ORF3a expression in driving neurological manifestations in the event of direct brain cell infection by SARS-CoV-2.

2 | RESULTS

2.1 | SARS-CoV-2 ORF3a is specifically expressed in the brains of AAV-ORF3a-injected mice

We used the AAV-PHP.eB serotype to broadly express SARS-CoV-2 ORF3a in the brain of mice. This AAV serotype efficiently crosses the blood-brain barrier to selectively deliver genes for expression in brain.²⁸ C57BL/6J mice at 6 weeks of age were injected via a retro-orbital route with either 1×10^{11} vg (Figure 1) or 2×10^{11} vg (Supporting Information Figure S1) AAV-PHP.eB carrying ORF3a (AAV-ORF3a) driven by a CAG (CMV early enhancer/chicken β -actin) promoter or an AAV-PHP.eB control (AAV-Control) containing an ORF-negative stuffer fragment under the same regulatory elements (Figure 1A). To avoid excessive protein expression, we used relatively low systemic AAV doses.²⁹ Mice were euthanized for analysis 2 weeks after receiving the high dose and 3 weeks after receiving the low dose due to the more rapid decline in the health condition of the mice injected with the high dose. Brain, lung, liver, and kidney tissue were examined by Western blotting to identify ORF3a protein expression (Figure 1B, Supporting Information Figure S1A). Expression of ORF3a protein, observed as multiple bands between 30 and 40 kDa presumably due

FIGURE 1 SARS-CoV-2 ORF3a is specifically expressed in the brains of AAV-ORF3a-injected mice. (A) Schematic of basic experimental design for analysis of forced SARS-CoV-2 ORF3a expression in mouse tissues. (B–G) Mice were injected with 1×10^{11} vg of AAV-ORF3a or AAV-Control. Mice were euthanized 3 weeks after the injection, and tissues harvested and prepared for Western blotting or immunohistology. (B) Western blot of mouse brain, lung, liver, and kidney extracts. Top: ORF3a and β -actin blots of tissues of three AAV-ORF3a-injected mice and one representative AAV-Control-injected mouse. Bottom: Quantification of the Western blots. ORF3a levels were normalized to β -actin levels detected on the same blot. The mean ORF3a level in brain was set to 100%. Data are expressed as means \pm SD ($n = 3$ for AAV-ORF3a-injected and AAV-Control mice). (C) Representative images of sagittal sections of brains stained with antibody to ORF3a (green), with DAPI (blue) nuclear counterstaining. Scale bar, 1 mm. (D) Representative images of a brain-stem section from an AAV-ORF3a-injected mouse stained with antibodies to ORF3a (green) and NeuN (red). Arrows identify cells expressing both ORF3a and NeuN. Scale bar, 20 μ m. (E) Representative images of a brain-stem section from an AAV-ORF3a-injected mouse stained with antibodies to ORF3a (green) and GFAP (red). Arrows identify cells expressing both ORF3a and GFAP. Scale bar, 20 μ m. (F) Representative images of a brain-stem section from an AAV-ORF3a-injected mouse stained with antibodies to ORF3a (green) and Olig2 (red). Arrows identify cells expressing both ORF3a and Olig2. Scale bar, 20 μ m. (G) Representative images of a brain-stem section from an AAV-ORF3a-injected mouse stained with antibodies to ORF3a (green) and Iba1 (red). Scale bar, 20 μ m.



to glycosylation heterogeneity,³⁰ was detected in the brain with comparatively little expression in lung, liver, or kidney of mice injected with AAV-ORF3a. No ORF3a protein was detected in the brain of mice injected with AAV-Control. These results confirm the specificity of the AAV-PHP.eB serotype for forcing brain expression of ORF3a.

To identify the extent of ORF3a expression in brain, sagittal sections cut from brain tissue harvested from

AAV-ORF3a- or AAV-Control-injected mice were stained with an ORF3a antibody (Figure 1C, Supporting Information Figure S1B). Widespread ORF3a expression was detected in the brains of AAV-ORF3a-injected mice, including in the cerebral cortex, midbrain, thalamus, pons, cerebellum, and medulla. The staining was specific, as indicated by the absence of ORF3a signal in stained brain sections from AAV-Control-injected mice.

In AAV-ORF3a-injected mice, ORF3a expression could be detected in NeuN-positive neurons (arrows: **Figure 1D**, Supporting Information **Figure S1C**), GFAP-positive astrocytes (arrows: **Figure 1E**, Supporting Information **Figure S1D**), and Olig2-positive oligodendrocytes (arrows: **Figure 1F**, Supporting Information **Figure S1E**). Iba1-positive microglia were largely devoid of ORF3a expression (**Figure 1G**, Supporting Information **Figure S1F**). The results indicate that ORF3a is specifically expressed in brain within neurons, astrocytes, and oligodendrocytes with either dose of AAV.

2.2 | SARS-CoV-2 ORF3a expression causes neurological disturbances

We evaluated mice injected with 1×10^{11} vg AAV-ORF3a or AAV-Control to determine if ORF3a expression affected neurological functions. Over the course of the 3 weeks after

injection, mice expressing ORF3a became severely debilitated, ultimately losing up to approximately 30% of their body weight and necessitating euthanasia (**Figure 2A**). Within 2 weeks after injection, the mice expressing ORF3a exhibited ataxic features (**Figure 2B**, Supporting Information **Figure S2**). Rotarod (**Figure 2C**) and wire-hanging testing (**Figure 2D**) demonstrated that the ORF3a-expressing mice were significantly impaired in balance, strength, and coordination compared with the control group. The results indicate that the forced ORF3a expression rapidly and severely impaired neurological functions.

2.3 | SARS-CoV-2 ORF3a expression causes neurodegeneration and cell death in the brain

SARS-CoV-2 has been reported to induce neuronal cell death.^{9,14} For this reason, we examined the mice injected

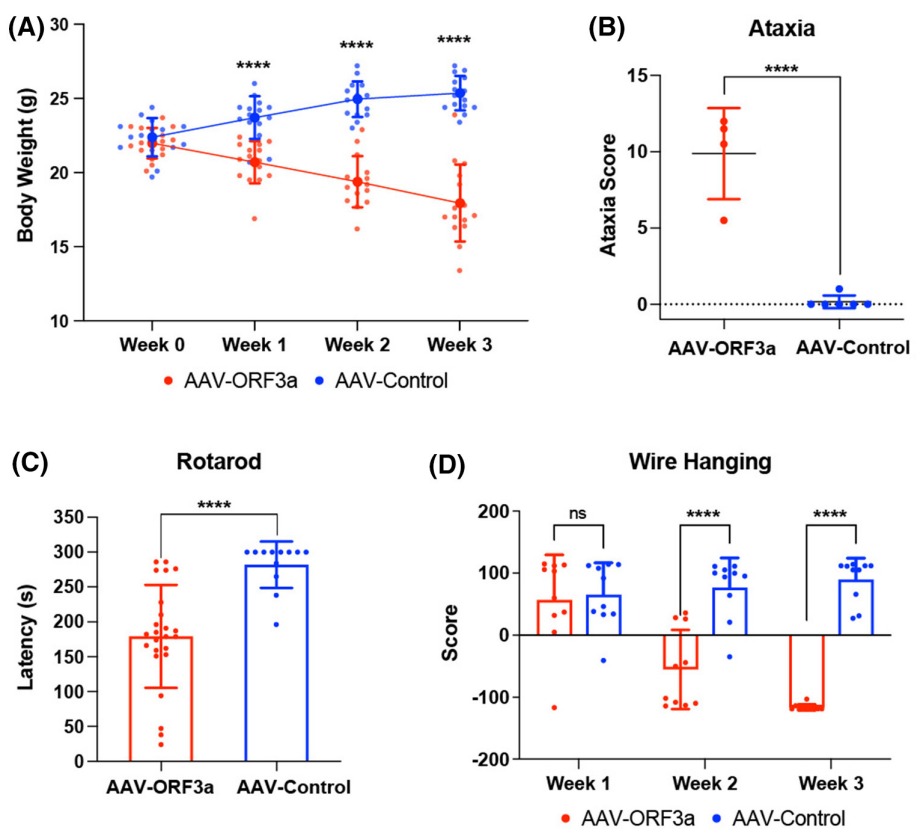


FIGURE 2 SARS-CoV-2 ORF3a expression causes neurological disturbances in AAV-ORF3a-injected mice. Mice were injected with 1×10^{11} vg AAV-ORF3a or AAV-Control, then assessed over 3 weeks for body weight and behavioral abnormalities. (A) Body weights of mice determined weekly for 3 weeks after injection. $n=15$ for AAV-ORF3a-injected and AAV-Control mice. (B) Aggregate ataxia score of mice 2 weeks after injection. Performance of mice on individual component measures of the ataxia analysis is presented in Supporting Information **S2**. $n=4$ for AAV-ORF3a-injected and $n=6$ for AAV-Control mice. (C) Latency time for mice to fall from an accelerating rotarod 2 weeks after injection. $n=8$ for AAV-ORF3a-injected and $n=4$ for AAV-Control mice. Three trials each mouse. (D) Performance of mice on wire-hanging test determined weekly for 3 weeks after injection. $n=10$ for AAV-ORF3a-injected and AAV-Control mice. Data are expressed as means \pm SD; **** $p < .0001$. ns, not significant.

with AAV-ORF3a or AAV-Control for histological evidence of neurodegeneration. Brain sections were subjected to a silver-staining method (NeuroSilver) that detects degenerating neuronal soma, axons, and terminals.³¹ Increased silver-grain deposition, indicative of neurodegeneration, was widespread on sagittal brain sections of AAV-ORF3a-injected mice when compared with sections from AAV-Control-injected mice (Figure 3A, Supporting Information Figure S3A). In the ORF3a-expressing brains, intense silver staining was observed in the cerebral cortex (Supporting Information Figure S3B), hippocampus (Figure 3B), in axons in the white matter in cerebellum and corpus callosum (Figure 3C, Supporting Information Figure S3C), and in the Purkinje cell layer and molecular layer of the cerebellum (Figure 3D). Quantification of the silver-staining density in the cortex region revealed an approximately 20-fold increase in ORF3a-expressing brains compared with the cortex region from control brains (Figure 3E).

We used TUNEL assays³² to determine if the level of apoptosis in the brain was increased because of ORF3a expression. A significantly increased number of TUNEL-positive cells were present in the thalamus of brains of mice expressing ORF3a compared with the brains from control mice (Figure 3F,G). TUNEL-positive cells colocalized with ORF3a expression (Figure 3H) and with the neuron marker NeuN (Figure 3I). These results show that ORF3a expression in the brain causes widespread neurodegeneration and neuronal apoptosis.

2.4 | SARS-CoV-2 ORF3a expression causes glial cell responses in the brain

Glial activation and inflammatory cytokine expression are key features of neuropathogenesis associated with SARS-CoV-2 infection.^{33,34} To explore the possible effects of ORF3a on glial activation, we examined glial cells in the brains of mice injected with AAV-ORF3a or AAV-Control. Iba1 immunostaining, which detects microglia, was increased in intensity throughout the brains of mice injected with AAV-ORF3a compared with mice injected with AAV-Control (Figure 4A, Supporting Information Figure S3D). The microglia in mice injected with AAV-ORF3a also displayed an enlarged morphology compared with what was observed in mice injected with AAV-Control, suggesting an activated state (Figure 4B, Supporting Information Figure S3E).³⁵ Quantitation of Iba1 fluorescence signal intensity in the cortex region revealed a significant increase in mice injected with AAV-ORF3a compared with mice injected with AAV-Control (Figure 4C).

GFAP immunostaining, which detects astrocytes, was also more intense throughout the brains of mice injected with AAV-ORF3a compared with mice injected

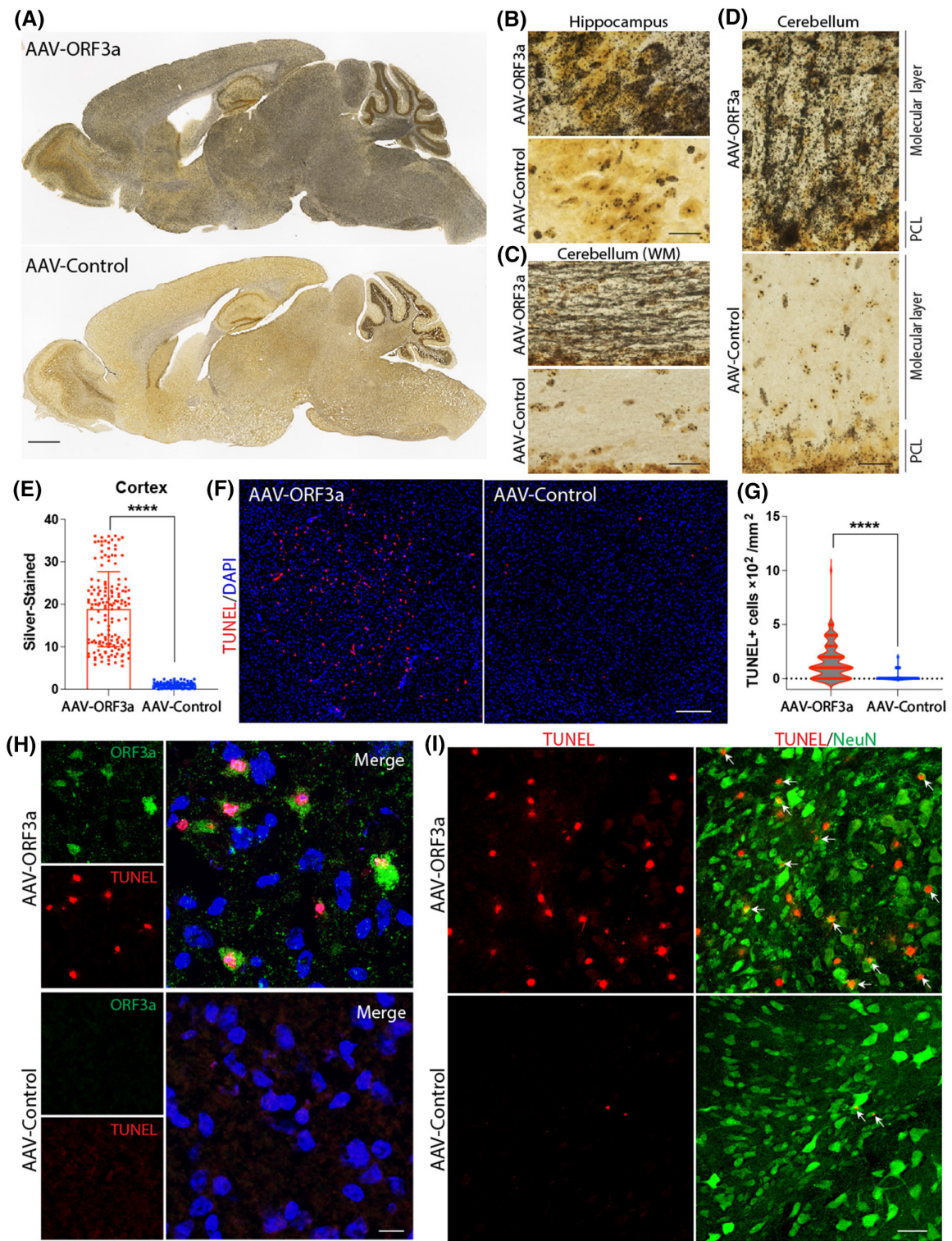
with AAV-Control (Figure 4D, Supporting Information Figure S3F). These astrocytes in mice injected with AAV-ORF3a were highly GFAP positive, with a hypertrophic morphology (Figure 4E, Supporting Information Figure S3G). Fluorescence intensity of GFAP staining in the brain stem was significantly increased in mice injected with AAV-ORF3a compared with mice injected with AAV-Control (Figure 4F). These features are consistent with an intense reactive glial response to the brain expression of ORF3a.

2.5 | SARS-CoV-2 ORF3a expression upregulates inflammatory genes in the brain

To investigate the effects of ORF3a on gene expression, we performed RNA-seq analysis on RNA isolated from the brains of mice 2 weeks after injection of 1×10^{11} vg AAV-ORF3a or AAV-Control. The expression of 861 genes was significantly increased, and 51 genes were significantly decreased in the ORF3a-expressing brains compared with the control brains (Figure 5A, Supplemental data). The Gene Ontology (GO) analysis of the differentially expressed genes revealed that the highest ranked Biological Process categories according to statistical significance were largely related to immune and inflammatory responses (Figure 5B). Cellular component categories included those with known sites of ORF3a action, including inflammasome complex,²³ lysosome,^{19,20} and MHC protein complex³⁶ (Figure 5C). Most molecular function categories were related to cytokine and chemokine pathways (Figure 5D). The heatmap of the differentially expressed genes within the GO: cytokine activity category demonstrated the broad elevation of cytokine RNAs in the ORF3a-expressing brains compared with the control brains (Figure 5E). These included for pro-inflammatory cytokines RNAs for TNF- α (Tnf), IL-1 β (Il1b), MCP-1 (Ccl2), and MIP-1 β (Ccl4), which have all been found to be elevated in cerebrospinal fluid of individuals with SARS-CoV-2 infection.^{33,37} These results suggest that ORF3a produces an inflammatory response in the brain.

2.6 | SARS-CoV-2 ORF3a expression disrupts the autophagy–lysosomal pathway in the brain

ORF3a has been reported to inhibit the fusion of autophagosomes with lysosomes, thereby disrupting autophagic progression.²⁰ To determine if ORF3a expression impairs autophagy in the brain, we utilized transgenic mice that express GFP-LC3B (microtubule-associated protein 1 light chain 3 beta) to visualize autophagosomes in



brain sections as green, fluorescent puncta³⁸ (Figure 6A). When autophagy progression is blocked, the GFP-labeled autophagosomes accumulate.³⁸ GFP-LC3B transgenic mice were injected with 1×10^{11} vg AAV-ORF3a or AAV-Control and examined for the GFP signal in brain tissue, which would indicate autophagosome abundance. Sagittal brain sections from GFP-LC3B transgenic mice injected

with AAV-ORF3a showed increased levels of GFP fluorescence in the cortex, thalamus, cerebellum, and brain stem when compared with GFP-LC3B transgenic mice injected with AAV-Control (Figure 6B). Within the cerebellum of AAV-ORF3a-injected mice, increased GFP-LC3B fluorescence was especially prominent in the granular layer and white matter (Figure 6C). In the cerebral cortex of

FIGURE 3 SARS-CoV-2 ORF3a expression causes neurodegeneration and cell death in the brains of AAV-ORF3a-injected mice. Mice were injected with 2×10^{11} vg of AAV-ORF3a or AAV-Control. Mice were euthanized 20 days ($n=3$) (panels A–E) or 14 days ($n=3$) (panels F–I) after the injection, and brains harvested and prepared for immunohistology or histochemistry. (A) Representative images of sagittal sections of brains stained by the NeuroSilver method. Scale bar, 1 mm. (B) Representative images of NeuroSilver staining of neurons in CA3 region of hippocampus sections. Scale bar, 20 μ m. (C) Representative images of NeuroSilver staining of axons in white matter (WM) of cerebellum sections. Scale bar, 20 μ m. (D) Representative images of NeuroSilver staining of Purkinje cells (soma and dendrites) in cerebellum sections. PCL: Purkinje cell layer. Scale bar, 20 μ m. (E) Quantification of silver-grain deposition in the cerebral cortex. Data are expressed as means \pm SD; **** $p < .0001$. (F) Representative images of TUNEL staining of brain (thalamus) sections, with DAPI (blue) nuclear counterstaining. Scale bar, 300 μ m. (G) Quantification of TUNEL-positive cells in brain (thalamus) sections ($n=3$). **** $p < .0001$. (H) Representative images of ORF3a immunostaining (green) and TUNEL staining (red) of brain (thalamus) sections, with DAPI (blue) nuclear counterstaining. Scale bar, 10 μ m. (I) Representative images of NeuN immunostaining (green) and TUNEL staining (red) of brain-stem sections. Arrows identify TUNEL positive cells expressing NeuN. Scale bar, 50 μ m.

AAV-ORF3a-injected mice, the GFP-LC3B fluorescence intensity was significantly increased compared with the cortex in mice injected with AAV-Control (Figure 6D,E). The results indicate that elevated numbers of autophagosomes are associated with ORF3a expression in the brain.

To determine if increased numbers of autophagosomes may be due to a block in autophagy progression, we measured levels of p62, a receptor that links cargo to autophagic membranes and is degraded during autophagic flux.³⁹ When autophagy progression is blocked, p62 will accumulate. Western blot analysis demonstrated that brains from AAV-ORF3a-injected mice expressed significantly increased levels of p62 compared with brains from AAV-Control-injected mice (Figure 6F). Together with the previous experiment, these results indicate that ORF3a expression in the brain blocks autophagic progression, possibly through its known action of inhibiting autophagosome-lysosome fusion,²⁰ resulting in the accumulation of autophagosomes.

The autophagy-lysosomal pathway plays an important role in the clearance of α -synuclein,⁴⁰ a neuronal protein implicated in neurodegenerative disease.²⁷ To further explore the effects of ORF3a on the autophagy-lysosomal pathway in the brain, we determined if levels of α -synuclein were disturbed after ORF3a expression. Immunostaining demonstrated that α -synuclein levels were significantly increased in brain-stem neurons of AAV-ORF3a-injected mice compared with neurons from AAV-Control-injected mice (Figure 6G,H).

In brain, Lamp1 is expressed on organellar intermediates of autophagic pathways and lysosomal biogenesis.⁴¹ To examine the relationship between Lamp1 and ORF3a, we investigated Lamp1 expression in brain tissue of AAV-ORF3a-injected and AAV-Control-injected mice. Lamp1 expression was increased in brain sections from AAV-ORF3a-injected mice compared with what was observed for mice injected with AAV-Control (Supporting Information Figure S4A,B). Western blots confirmed a significant increase in Lamp1 expression in the brains of AAV-ORF3a-injected mice compared with AAV-Control-injected mice

(Supporting Information Figure S4C). Furthermore, ORF3a was found to partially co-localize with Lamp1 in the brain of AAV-ORF3a-injected mice (Supporting Information Figure S4D). Collectively, these results indicate that ORF3a coincides with and disturbs the autophagy-lysosomal pathway in brain.

2.7 | SARS-CoV-2 ORF3a expression causes accumulation of glycosphingolipids in the brain

In lysosomal storage diseases in which the autophagy-lysosomal pathway is defective, the glycosphingolipids GM2 ganglioside and GM3 ganglioside, which are intermediates in the ganglioside-degradation pathway (Figure 7A), often accumulate in neurons.²⁴ To examine what effect ORF3a expression in brain would have on glycosphingolipid levels, we analyzed the levels of gangliosides in brain tissue from AAV-ORF3a-injected and AAV-Control-injected mice. High-performance thin-layer chromatography (HPTLC) analysis of gangliosides revealed that levels of GM1, GM2, and GM3 gangliosides were significantly increased in brains of mice injected with AAV-ORF3a compared with mice injected with AAV-Control (Figure 7B,C). Immunostaining demonstrated intracellular GM2 ganglioside accumulation in NeuN-positive neurons in the cerebral cortex of AAV-ORF3a-injected mice (Figure 7D). These results suggest that ORF3a expression in the brain impedes the degradation of brain gangliosides, providing further evidence that ORF3a disrupts lysosomal function in the brain.

2.8 | SARS-CoV-2 ORF3a expression directly disrupts cellular glycosphingolipid metabolism

To determine if ORF3a expression directly disrupts cellular glycosphingolipid homeostasis, we established

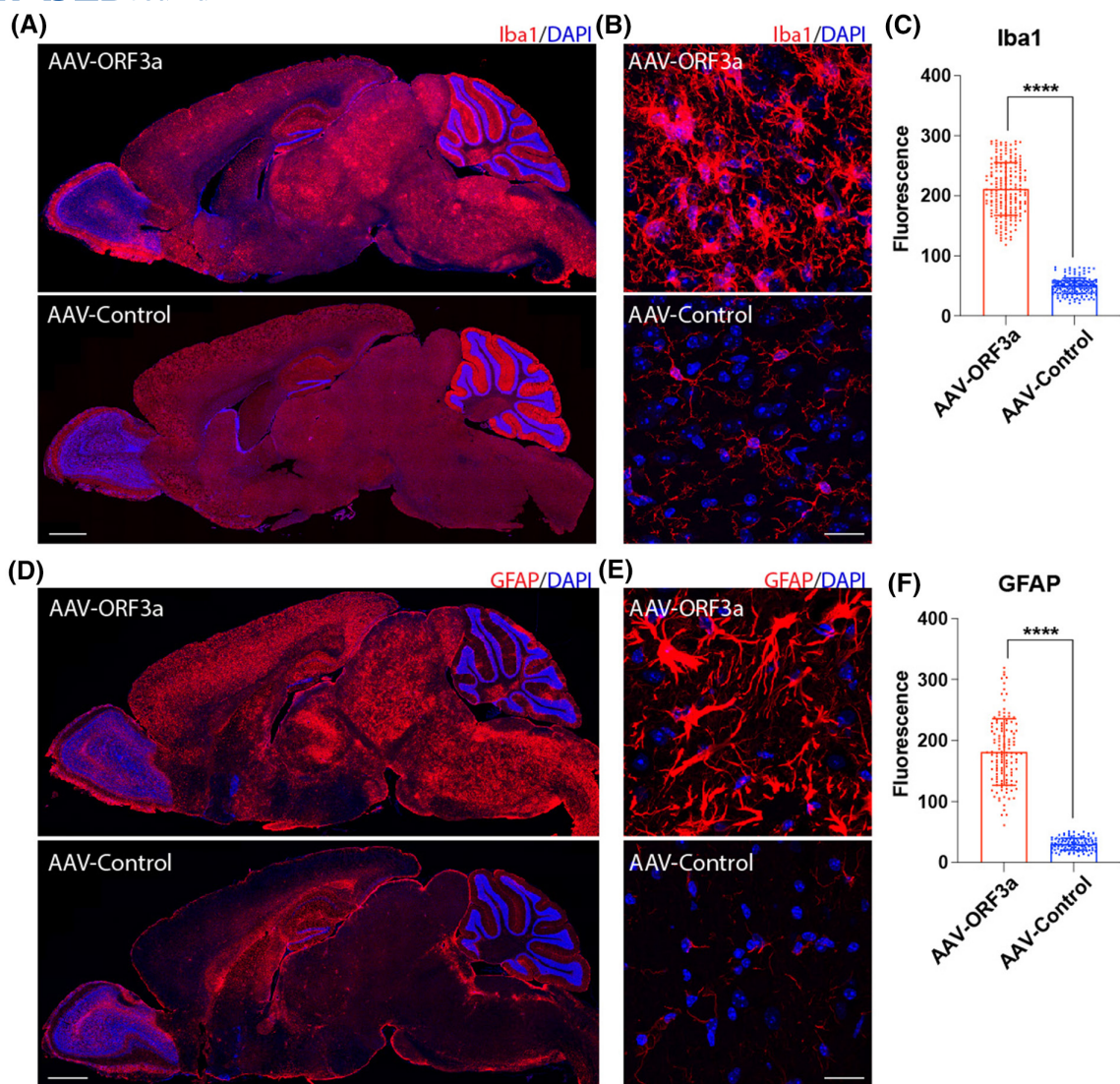


FIGURE 4 SARS-CoV-2 ORF3a expression causes glial cell responses in the brains of AAV-ORF3a-injected mice. Mice were injected with 2×10^{11} vg of AAV-ORF3a ($n=3$) or AAV-Control ($n=3$). Mice were euthanized 2 weeks after the injection, and brains harvested and prepared for immunohistology. (A) Representative images of sagittal sections of brains stained with antibody to Iba1, with DAPI (blue) nuclear counterstaining. Scale bar, 1 mm. (B) Representative images of cerebral-cortex sections stained with antibody to Iba1, with DAPI (blue) nuclear counterstaining. Scale bar, 20 μ m. (C) Quantification of Iba1 fluorescence intensity in the cerebral cortex. Data are expressed as means \pm SD; *** $p < .0001$. (D) Representative images of sagittal sections stained with antibody to GFAP, with DAPI (blue) nuclear counterstaining. Scale bar, 1 mm. (E) Representative images of brain-stem sections stained with antibody to GFAP, with DAPI (blue) nuclear counterstaining. Scale bar, 20 μ m. (F) Quantification of GFAP fluorescence intensity in brain-stem sections. Data are expressed as means \pm SD; *** $p < .0001$.

ORF3a-expressing (ORF3a-HeLa) and Control-HeLa cell lines. First, we tested the functionality of the autophagy pathway in the cell lines. We used an autophagy sensor (RFP-GFP-LC3B; Figure 8A) in which the RFP fluorescence is acid stable and the GFP fluorescence is acid sensitive. The conversion from autophagosome (neutral pH) to autolysosome (acidic pH) can be visualized by imaging the loss of the GFP fluorescence, with retention of RFP fluorescence, that occurs upon acidification of the autophagosome following lysosomal fusion. Compared with Control-HeLa cells, the ORF3a-HeLa cells contained

a significantly increased number of punctate structures with both green and red fluorescence, indicating that the conversion of autophagosomes to autolysosomes was indeed blocked (Figure 8B,C).

To probe the sphingolipid transport and degradation pathways in ORF3a-HeLa and Control-HeLa cells, we utilized BODIPY™ FL C₅-Lactosylceramide (BODIPY-LacCer), a fluorescently labeled glycosphingolipid (Figure 8D). In cells with a normal lysosomal-degradation pathway, the BODIPY-LacCer accumulates in the Golgi apparatus, while in cells with defects in sphingolipid degradation,

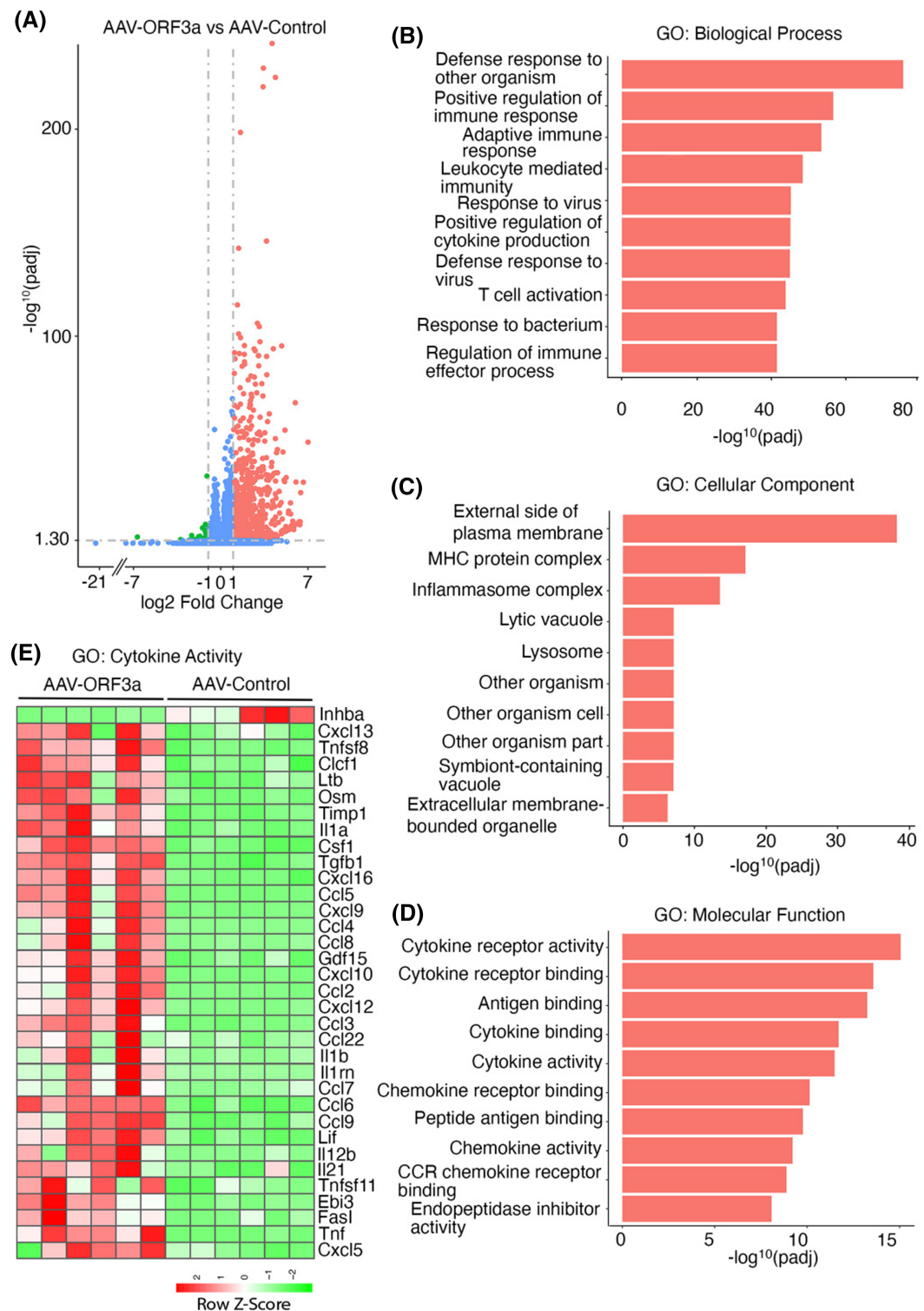


FIGURE 5 SARS-CoV-2 ORF3a expression upregulates inflammatory genes in the brains of AAV-ORF3a-injected mice. Mice were injected with 1×10^{11} vg of AAV-ORF3a ($n=6$) or AAV-Control ($n=6$). Mice were euthanized 3 weeks after the injection, brains harvested, and RNA isolated for RNA-seq analysis. (A) Volcano plot showing significantly differentially expressed genes in brains from AAV-ORF3a-injected mice compared with AAV-Control-injected mice. Genes significantly upregulated (\log_2 fold change $> +1$) in AAV-ORF3a are shown in red. Genes significantly downregulated (\log_2 fold change > -1) are shown in green. Genes with expression levels not significantly different or between \log_2 fold change -1 and $+1$ are shown in blue. (B–D) Top 10 GO: Biological Process (B), cellular component (C), and molecular function (D) categories that are differentially regulated by ORF3a expression. (E) Heatmap indicating the row Z-score of individual genes in the GO: cytokine activity category. Each vertical column represents an individual mouse.

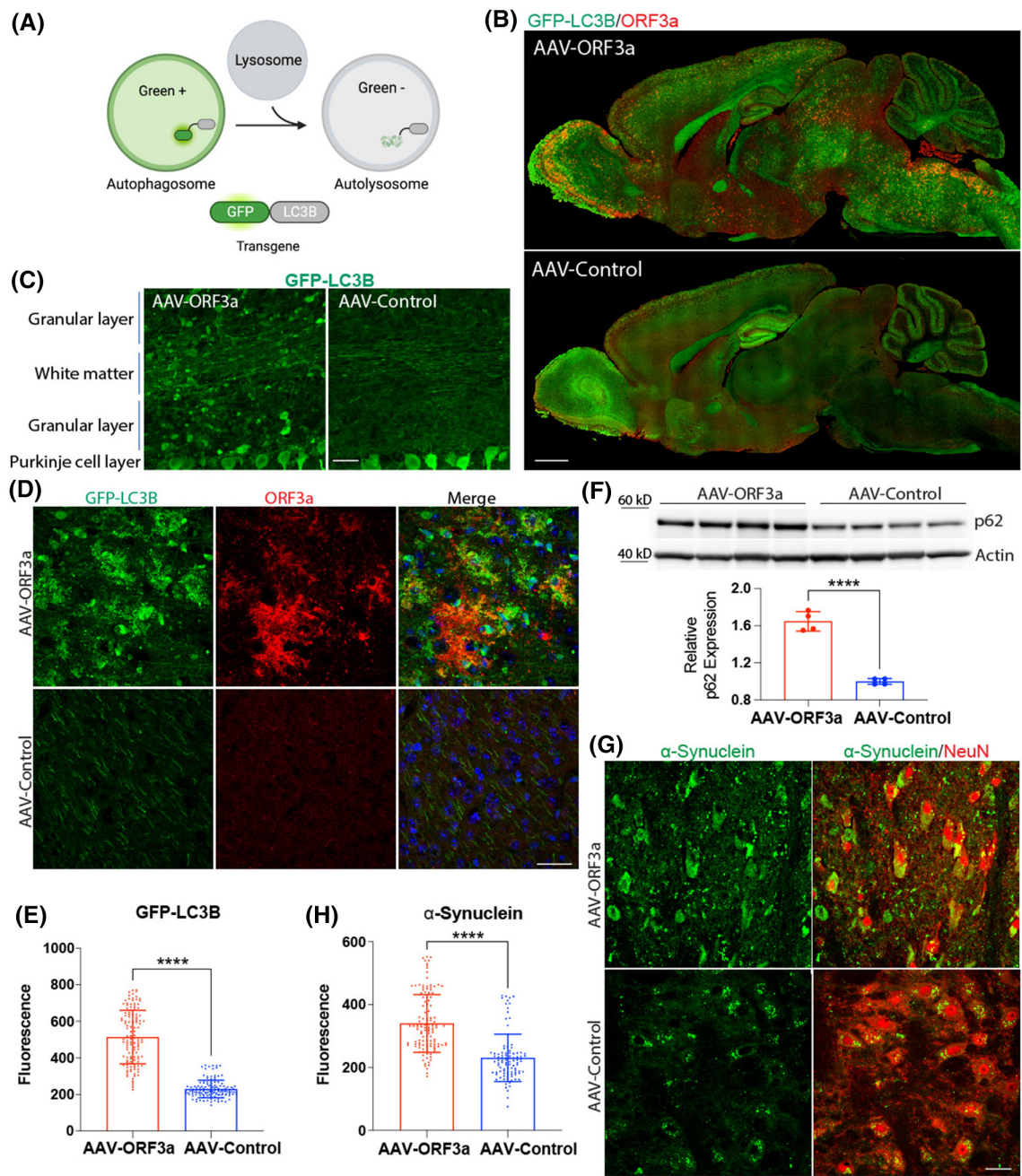


FIGURE 6 SARS-CoV-2 ORF3a expression disrupts the autophagy-lysosomal pathway in the brains of AAV-ORF3a-injected mice. (A) Schematic of the mechanism by which the GFP-LC3B transgene was used for visualizing autophagosomes. (B-E) GFP-LC3B C57BL/6 mice³⁸ (6 weeks old) were injected with 1×10^{11} vg AAV-ORF3a ($n = 6$) or AAV-Control ($n = 6$). Mice were euthanized 5 weeks after the injection, and brains harvested and sectioned. (B) Representative images of sagittal sections stained with antibody to ORF3a (red). Endogenous GFP-LC3B transgene expression is visualized as green. Scale bar, 1 mm. (C) Representative images of cerebellum sections. Endogenous GFP-LC3B is green. Scale bar, 30 μ m. (D) Representative images of cerebral-cortex sections stained with antibody to ORF3a (red). Endogenous GFP-LC3B is green. Scale bar, 30 μ m. (E) Quantification of GFP-LC3B fluorescence intensity in cerebral-cortex sections. Data are expressed as means \pm SD; **** p < .0001. (F) C57BL/6J mice were injected with 1×10^{11} vg AAV-ORF3a ($n = 4$) or AAV-Control ($n = 4$). Mice were euthanized 3 weeks after the injection, and brains harvested and prepared for Western blotting. Top: ORF3a and β -actin blots of brain extracts. Bottom: Quantification of the Western blots. p62 levels were normalized to β -actin levels detected on the same blot. Data are expressed as means \pm SD; **** p < .0001. (G, H) GFP-LC3B C57BL/6 mice³⁸ (6 weeks old) were injected with 1×10^{11} vg AAV-ORF3a ($n = 6$) or AAV-Control ($n = 6$). Mice were euthanized 5 weeks after the injection, and brains harvested and prepared for immunohistology. (G) Representative images of brain-stem sections stained with antibodies to α -synuclein (green) and NeuN (red). Scale bar, 30 μ m. (H) Quantification of α -synuclein fluorescence intensity in brain-stem sections. Data are expressed as means \pm SD; **** p < .0001.

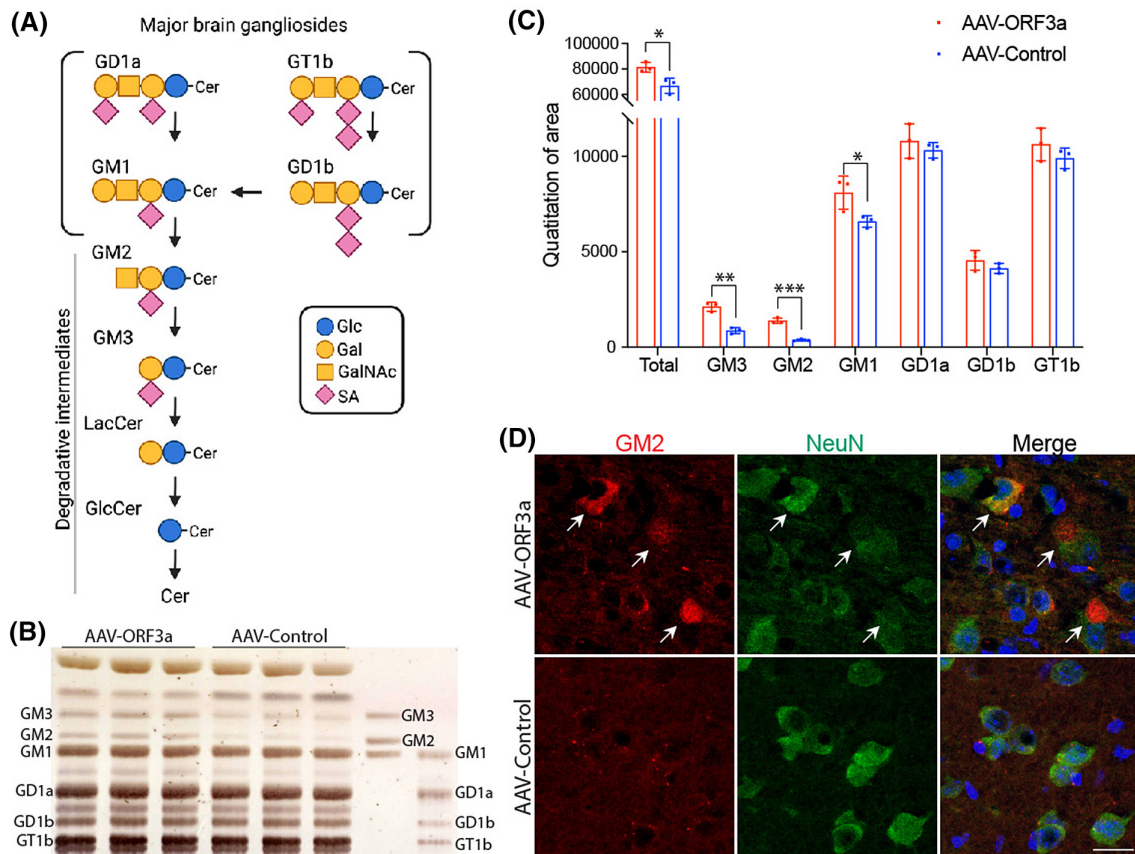
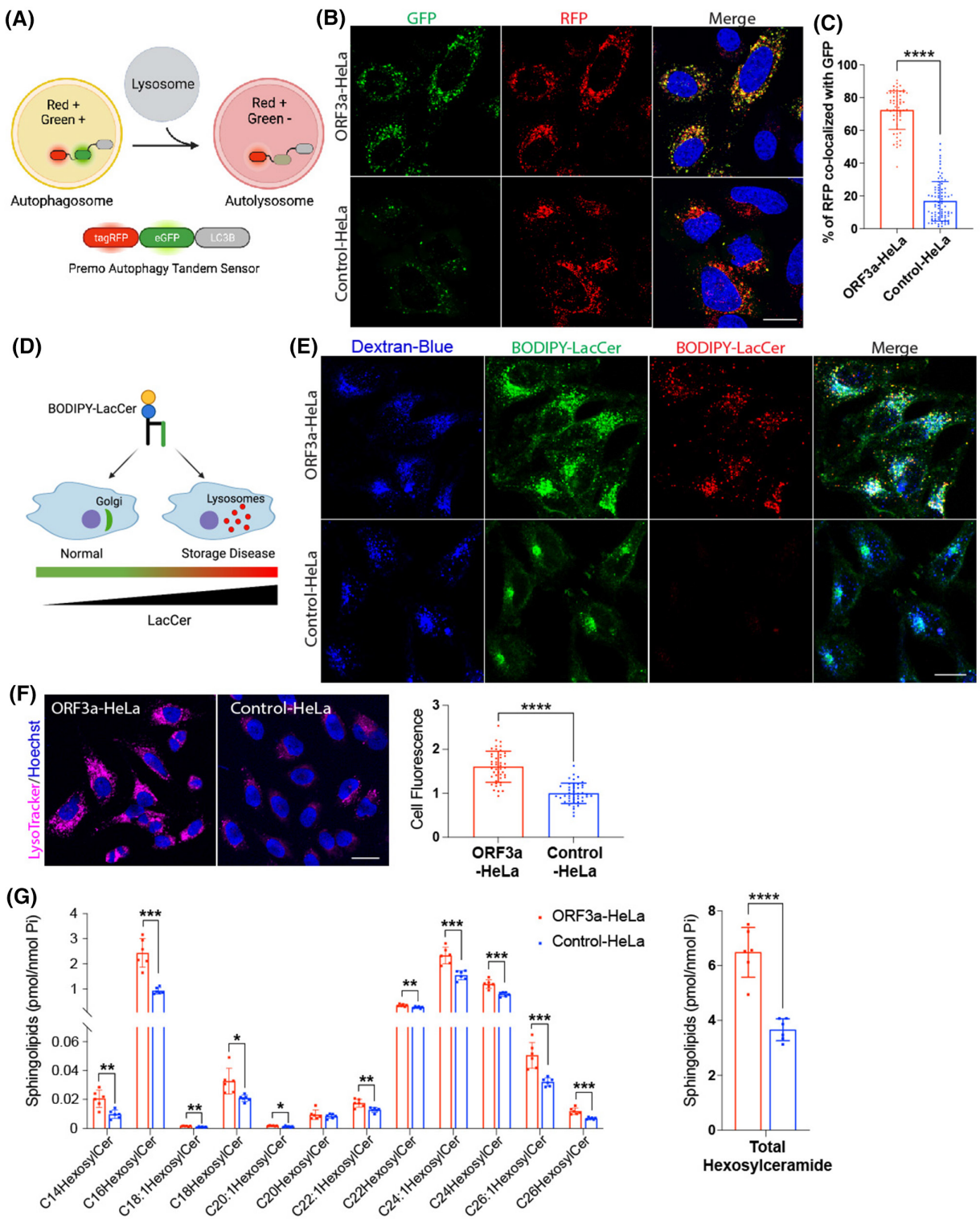


FIGURE 7 SARS-CoV-2 ORF3a expression causes accumulation of glycosphingolipids in the brains of AAV-ORF3a-injected mice. (A) Schematic illustrating the structures of major brain gangliosides and their degradative intermediates. (B–D) Mice were injected with 1×10^{11} vg of AAV-ORF3a ($n = 3$) or AAV-Control ($n = 3$). Mice were euthanized 2 weeks after the injection, and brains harvested and prepared for lipid analyses or immunohistology. (B) HPTLC analysis of brain gangliosides. The positions of the ganglioside standards are indicated on the right. (C) Quantification of ganglioside band intensities from HPTLC analysis. Data are expressed as means \pm SD * $p < .05$, ** $p < .01$, *** $p < .001$. (D) Representative images of cerebral-cortex sections stained with antibodies to GM2 ganglioside (red) and NeuN (green). Arrows indicate neurons that are positive for intracellular GM2 ganglioside. Scale bar, 20 μm.

the BODIPY-LacCer accumulates in late endosomes and lysosomes, with a shift in fluorescence from green to red wavelengths due to an increased local concentration.^{42–44} In the Control-HeLa cells pulsed with BODIPY-LacCer, green fluorescence was detected in a Golgi-like pattern consistent with normal cellular sphingolipid handling (Figure 8E). ORF3a-HeLa cells pulsed with BODIPY-LacCer produced a punctate green fluorescent pattern that coincided with the dextran-blue lysosomal marker (Figure 8E). In contrast to the Control-HeLa cells, the BODIPY-LacCer signal in the ORF3a-HeLa cells exhibited a shift to red fluorescence, indicating an elevated concentration (Figure 8E). The impaired BODIPY-LacCer trafficking and its accumulation suggest that ORF3a expression caused a block in lysosomal glycosphingolipid trafficking and degradation. To explore lysosomal dysfunction in ORF3a-HeLa cells further, we employed the LysoTracker biomarker. Relative acidic compartment volume expansion as measured by LysoTracker staining has been shown to be a biomarker for impaired

lysosomal function in lysosomal storage diseases.⁴⁵ ORF3a-HeLa cells displayed significantly increased LysoTracker fluorescence compared with Control-HeLa cells (Figure 8F), indicating expansion of the lysosomal compartment in these ORF3a-expressing cells that may coincide with lysosomal dysfunction.

If glycosphingolipid degradation was indeed impaired by ORF3a expression, we would expect that endogenously synthesized glycosphingolipids would accumulate in ORF3a-expressing cells. Accordingly, we measured the levels of hexosylceramides in ORF3a-HeLa and Control-HeLa cells by HPLC-tandem mass spectrometry to determine if ORF3a expression affected their accumulation. Levels of hexosylceramides were significantly elevated in ORF3a-HeLa cells compared with Control-HeLa cells (Figure 8G). These results indicate that ORF3a expression disrupts the autophagy-lysosomal pathway and causes the cellular accumulation of glycosphingolipids.



3 | DISCUSSION

Here, we demonstrate that the SARS-CoV-2 accessory protein ORF3a, when expressed in brain, rapidly causes severe neurological impairment in mice. Forced ORF3a expression in murine brain via AAV-PHP.eB induced neurodegeneration and cell death, reactive microglia and

astrocytes, and upregulation of inflammatory cytokine genes. These coincide with the central neuropathological features that have been identified in the brains of patients and nonhuman primates infected with SARS-CoV-2.^{7,11} Furthermore, ORF3a expression disrupted the autophagy–lysosomal pathway, whose function is vital both for proper neurological function and for providing

FIGURE 8 SARS-CoV-2 ORF3a expression directly disrupts cellular glycosphingolipid metabolism in ORF3a-expressing HeLa cells. (A) Schematic of autophagy sensor system. HeLa cells were transduced with the Premo Autophagy Tandem Sensor (RFP-GFP-LC3B) to monitor the maturation of autophagosomes to autolysosomes. Autophagosomes express both GFP and RFP fluorescence. Autolysosomes express only RFP fluorescence, because GFP fluorescence is quenched by their characteristic acidic pH. (B) Representative images of GFP (green) and RFP (red) fluorescence in cells transduced with RFP-GFP-LC3B autophagy sensor. Cell nuclei were counterstained with Hoechst (in blue). Scale bar, 20 μm. (C) Quantification of percentage of RFP fluorescence co-localized with GFP fluorescence. Data are expressed as means ± SD; ***p < .0001. (D) Schematic of BODIPY-LacCer probe used for analysis of glycosphingolipid metabolism. In normal cells the probe is concentrated in the Golgi. In cells with a lysosomal storage defect, the probe is localized to lysosomes. The fluorescence of BODIPY-LacCer shifts from green to red wavelengths when its local concentration is increased. (E) Representative images of cells treated with BODIPY-LacCer (green and red fluorescence) and dextran-blue (blue fluorescence). Scale bar, 20 μm. (F) Representative images of cells treated with LysoTracker Deep Red (purple). Cell nuclei were counterstained with Hoechst (in blue). Scale bar, 30 μm. Fluorescence intensity of LysoTracker was quantified in each single cell. The mean Control-Hela was set to 1.0. Data are expressed as means ± SD, ***p < .0001. (G) Left: Individual hexosylceramide subspecies with different fatty-acid chain lengths, as indicated, and C18 sphingoid bases were determined by HPLC-tandem mass spectrometry on lipid extracts from cell samples (n = 6). Right: Total hexosylceramides with C18 sphingoid bases from cell samples. Data were normalized to inorganic phosphate (Pi). Data are expressed as means ± SD. Multiple unpaired t test; *p < .05, **p < .01, ***p < .001, ****p < .0001.

resilience to neurodegenerative disease.^{25,46} These results suggest that in the event of neuroinvasion by SARS-CoV-2, ORF3a expression in brain cells may acutely drive neuropathogenesis and increase vulnerability to neurodegenerative disease.

Along with indirect mechanisms, such as systemic inflammation, the generation of neuron-specific auto-antibodies, and hypoxic injury, direct SARS-CoV-2 neuroinvasion is considered as a possible neuropathological mechanism in COVID-19, although widespread CNS infection is not considered likely.^{1,3} The contribution of direct infection of brain cells to the neuropathogenesis in COVID-19 has been difficult to determine because of the dissemination of the virus to multiple organs (including the brain), the broad tropism, and complex pathogenesis. To understand the potential consequences of SARS-CoV-2 infection of cells within the brain, we utilized a brain-selective AAV-PHP.eB serotype in mice to express a key SARS-CoV-2 pathogenesis gene, ORF3a.

ORF3a has intrinsic activities that contribute to its role as a pathogenesis factor in COVID-19. First, it induces cell-death pathways, including apoptosis and necrosis, in a wide range of cultured cell types and in *Drosophila*.^{21,22,47} Second, it is a potent cell inducer of pro-inflammatory responses that trigger the release of cytokines and chemokines, possibly contributing to the “cytokine storm” in COVID-19.^{23,48} Finally, ORF3a disables the autophagy–lysosomal pathway, a key pathway that is required for efficient turnover of cellular constituents and viral clearance.^{19,20}

ORF3a inhibits the fusion of autophagosomes with lysosomes through an interaction with the homotypic fusion and protein sorting (HOPS) complex.²⁰ By blocking the autophagy–lysosomal pathway, ORF3a suppresses the intracellular clearance of SARS-CoV-2 and facilitates its export.¹⁹ In the present study, ORF3a expression

in the brain disrupted the autophagy–lysosomal pathway as evidenced by increased levels of LC3B and p62 in AAV-ORF3a-injected mice, suggesting impaired autophagosome–lysosome fusion. In line with a block in the autophagy–lysosomal pathway, we found that ORF3a-expressing brain contained abnormal accumulations of gangliosides GM3 and GM2, 2 intermediates in the degradation pathway of gangliosides that are often present at elevated levels in lysosomal storage diseases and other neurodegenerative disorders.^{24,26,49–51} We also observed that expression of α-synuclein, whose levels are maintained by autophagy and lysosomal degradation,⁴⁰ was increased in neurons in ORF3a-expressing brain.

Alzheimer’s and Parkinson’s disease, and frontotemporal dementia –all of which are neurodegenerative diseases–have underlying defects in autophagy–lysosomal pathway.^{25,26,46} Disruption of the autophagy–lysosomal pathway by ORF3a could potentially increase the levels of toxic protein aggregates associated with pathogenesis in Alzheimer’s and Parkinson’s diseases, as well as increase the levels of glycosphingolipids, as has been recently identified in frontotemporal dementia.²⁶ Focal β-amyloid deposits, which are characteristic of Alzheimer’s disease, have been found in the neocortex of young patients who succumbed to COVID-19.⁵² Intracellular α-synuclein aggregates, which are typically present in Parkinson’s disease patients, have been observed in the brains of SARS-CoV-2-infected macaques.⁵³ In SARS-CoV-2-infected hamsters, neurodegenerative processes initiated in the olfactory bulb caused accumulation of hyperphosphorylated tau and α-synuclein protein in cortical neurons.⁵⁴ Even a low frequency of infected neurons with ORF3a-induced autophagy–lysosomal pathway impairment could initiate the formation of pathological protein aggregates that could have the propensity to propagate and trigger wider neuropathology over time.

Gangliosides, which are increased during SARS-CoV2 infection,⁵⁵ have been previously implicated in pathogenesis. An association of COVID-19 with the neurological disease Guillain Barre syndrome has been reported.⁵⁶ Anti-ganglioside antibodies, which are often produced during Guillain Barre syndrome and have been detected in case studies of COVID-19 patients, may contribute to neurological manifestations.^{57,58} Furthermore, gangliosides have also been found to facilitate SAR-CoV2 virus entry into cells.⁵⁹ These findings indicate that increased levels of gangliosides resulting from ORF3a expression could enhance the spread of COVID-19 virus and potentially lead to immune-mediated neuropathogenesis.

A limitation of the current study stems from the use of AAV to express ORF3a and not an authentic SARS-CoV-2 virus. While this approach allows for an isolation of the ORF3a effect in the brain, the method does not emulate the natural entry route, timing, and regulation of expression that occurs during an authentic SARS-CoV-2 infection. The AAV method resulted in the expression of ORF3a in the brain more broadly than likely occurs during a SARS-CoV-2 infection. Thus, the extent of the neuropathology observed would be expected to exceed that which typically occurs during expression of ORF3a by SARS-CoV-2. Several interrelated processes contributing to neuropathogenesis were observed including neuroinflammation, neuronal cell death, impairment of the autophagy–lysosomal pathway with storage of glycosphingolipids and α -synuclein and neuronal apoptosis. However, the temporal and functional relationship between these processes during neuropathogenesis was not defined.

Our study illuminates a potentially important role for ORF3a in mediating both short- and long-term neurological manifestations of COVID-19. By disabling the autophagy–lysosomal pathway, ORF3a may also render the nervous system vulnerable to the onset of neurodegenerative disease. Reducing the possibility of ORF3a expression in the brain, either by preventing viral neuroinvasion or directly targeting ORF3a activity, may be an avenue to reduce the neurological consequences of SARS-CoV-2 infection.

4 | METHODS

4.1 | Mice

C57BL/6J mice were obtained from The Jackson Laboratory (Bar Harbor, ME). GFP-LC3B transgenic mice on a C57BL/6 background³⁸ were kindly provided by Dr. Noboru Mizushima, The University of Tokyo, Tokyo, Japan.

4.2 | Virus production

AAV vectors were constructed (Figure 1A) with the SARS-CoV-2 ORF3a sequence that included a 2xStrep tag contained within Addgene plasmid #141383 (Cambridge, MA)⁶⁰ or a 249 bp negative ORF control stuffer sequence (amino acids 2–83 of *Escherichia coli* β -galactosidase) driven by a CAG promoter. The control stuffer sequence contains no ATGs and would not be expected to produce a protein. WPRE (woodchuck hepatitis virus posttranscriptional regulatory element) and bovine growth hormone poly(A) sequences were added. Vector construction and virus packaging (serotype: AAV-PHP.eB) were performed by VectorBuilder (Chicago, IL).

Plasmid and lentiviral preparations encoding ORF3a (plasmid #141383, viral prep# 141383-LV (ORF3a-LV)) were purchased from Addgene. Control empty lentivirus vector, constructed by removing the ORF3a coding sequence from the Addgene plasmid #141383, and corresponding lentivirus (control-LV) preparation were produced by VectorBuilder.

4.3 | Retro-orbital injections

AAV-ORF3a or AAV-Control (low dose, 1×10^{11} vg per mouse; high dose, 2×10^{11} vg per mouse) preparations were diluted to 100 μ L PBS buffer (Fisher Scientific, Hampton, NH; Cat #BW17-516F, pH 7.4) before injection. Anesthesia was induced by 4% isoflurane in an induction chamber using an isoflurane vaporizer (IMPAC; VetEquip, Inc., Livermore, CA). Toe pinch was applied to monitor anesthetic depth. The right eyeball was partially protruded to the skin by applying gentle pressure with fingers. An insulin needle syringe (Becton Dickinson, Franklin Lakes, NJ; Cat #309306: 29-gauge, 0.5-inch) was introduced into the retrobulbar sinus with needle bevel down and the virus solution was injected slowly into the sinus.

Mouse tissues (brain, lung, liver, and kidney) were collected 2–5 weeks post-virus injection. Transcardial perfusion with saline (0.9% NaCl) was first performed to clear blood. The tissues from individual mice were divided for snap freezing with dry ice or fixation in 4% paraformaldehyde (in 0.1 M phosphate buffer, pH 7.4). The brain was hemisected in the midsagittal plane. Brain ORF3a expression was confirmed in all AAV-ORF3a-injected mice used in this study.

4.4 | Mouse behavioral analyses

The wire-hanging test, adapted from Jeyakumar et al.,⁶¹ was used to assess motor coordination and grip strength.

The apparatus consisted of a 26-cm rod suspended by two wooden beams 30 cm above a base platform covered with bedding. Mice were placed in the center of the rod, suspended by their forepaws. The time it took the mouse to either cross to the end of the rod or fall off was recorded. If a mouse hung for more than 120 s, the test was terminated. Scores were calculated using the following equations depending on whether the mouse crossed or fell: Score = 120 – cross time or Score = fall time – 120. Three trials were performed per mouse, and scores were averaged across the three trials.

Mouse ataxia scoring⁶² was done by the Murine Phenotyping Core Facility of the National Heart, Lung, and Blood Institute, NIH.

The accelerating-rotarod test was done with a rotarod apparatus for mice (Model #47600; Ugo Basile, Gemonio, Italy) to assess motor coordination, balance, and equilibrium. Before the test, mice were trained for 3 successive days at a fixed speed, starting with 4 rpm and gradually building up to 12 rpm (three trials/training, maximum 3 min/trial, with 10-min resting time between each trial). On the test day, the rotarod was set at an accelerating mode (4–40 rpm, 5 min), and the latency time for each mouse to fall from the rotarod was recorded. The test was repeated three times with at least 0.5 h of rest between each trial.

4.5 | RNA-seq

Brains from mice treated with 1×10^{11} vg AAV-ORF3a ($n=6$) or AAV-Control ($n=6$) were harvested 2 weeks after virus injection. ORF3a expression was confirmed by Western blot analysis. Total RNA from one brain hemisphere each was isolated using miRNeasy Mini Kit from Qiagen (Cat #217004; Redwood City, CA). Preparation of the RNA library, mRNA sequencing, and bioinformatic analysis was performed by Novogene (Beijing, China). Briefly, 3 µg of total RNA per sample was used as input for the RNA-seq analysis. Quality of RNA was verified using TapeStation (Agilent Technologies, Santa Clara, CA). Sequencing libraries were generated using NEBNext Ultra II RNA with PolyA Selection Kit (New England Biolabs, Ipswich, MA) following the manufacturer's protocol and sequenced on an Illumina PE150 (Illumina, San Diego, CA) for 40 million paired-end reads for each sample. Raw reads in FASTQ format were first processed to remove adapters, reads containing poly-N, and low-quality reads using fastp. At the same time, Q20, Q30, and GC content of the clean data were calculated. All high-quality clean reads were mapped to reference genome mm10 (GRCm38) using hisat2 2.0.5. Gene-expression quantification was performed using featureCounts 1.5.0-p3⁶³ and differential

analysis performed using DESeq2 1.20.0.⁶⁴ At least a 2.0-fold change ($\log_2(\text{fold-change}) > +1$ or < -1) in expression level with adjusted $p < .05$ were considered differentially expressed genes. Pathway enrichment GO and Kyoto Encyclopedia of Genes and Genomes (KEGG) analysis were performed using clusterProfiler 3.8.1⁶⁵ with corrected p -value set to $<.05$ for significant enrichment.

4.6 | Cell culture

HeLa cells (Cat #CCL-2; ATCC, Rockville, MD) were cultured in DMEM Glutamax (Cat #10569044; Thermo Fisher Scientific, Waltham, MA), 10% FBS with 100 U/mL Penicillin-Streptomycin (Cat #10140148; Thermo Fisher Scientific). Viral transduction was performed by plating 50 000 cells in a 24-well tissue culture plate to achieve 50%–70% confluence, then infecting them with lentiviral particles (ORF3a-LV and control-LV) at a MOI of 5. Puromycin (Thermo Fisher Scientific) was added 48 h post-transduction at 2 µg/mL for positive selection; cells were maintained in culture medium containing puromycin to prevent loss of gene expression. Cells were removed by trypsinization and washed with ice-cold PBS.

For BODIPY-LacCer labeling, HeLa cells were plated on 4-well µ-slides (Cat #80426; Ibidi, Gräfelfing, Germany) at a density of 20 000 cells/well. Cells were first incubated with Cascade Blue™-conjugated dextran (dextran-blue; Cat #D1976; Thermo Fisher Scientific) at 4 mg/mL in 10%FBS/DMEM Glutamax culture medium for 48 h at 37°C to label lysosomes. Cells were then incubated with 5 µM BODIPY-LacCer (Cat #B34402; Thermo Fisher Scientific) in HEPES-buffered DMEM without phenol red (HMEM; Cat #21063029; Thermo Fisher Scientific) for 1 h at 37°C. Cells were washed three times with ice-cold HMEM, then back-exchanged six times with 5% BSA in HMEM, 10 min each, at 11°C to remove excess BODIPY-LacCer. Cells were further incubated at 37°C for another 1 h, then chilled on ice for imaging under a Zeiss confocal microscope (Model LSM 780; Carl Zeiss Microscopy, White Plains, NY).

The Premo Autophagy tandem sensor RFP-GFP-LC3B kit (Cat #P36239; Thermo Fisher Scientific) was used to monitor the maturation of autophagosomes to autolysosomes in HeLa cells. Cells (20 000 cells/well) were plated on 4-well µ-slides and transduced with BecMam RFP-GFP-LC3B at 30 particles per cell overnight in 10%FBS/DMEM Glutamax culture medium. Cells were transferred into fresh culture medium and grown for another 24 h, then counterstained with Hoechst 33342 (Cat #H3570; Thermo Fisher Scientific) at 2 µg/mL for

30 min at 37°C. Alternatively, cells were co-stained with 50 nM LysoTracker™ Deep Red (Cat #L12492; Thermo Fisher Scientific) and Hoechst 33342 for 30 min at 37°C. After three brief washes with PBS, cells were incubated in HMEM and imaged under a Zeiss confocal microscope. The images were analyzed for co-localization of RFP and GFP with ZEN (Carl Zeiss Microscopy), greater than 60 cells from each group were analyzed for statistical comparison. Total cell fluorescence of LysoTracker staining was measured using Fiji/ImageJ,⁶⁶ around 45 cells from each group were analyzed.

4.7 | Immunohistology and histochemistry

Fixed mouse brain hemispheres were placed in 20% sucrose overnight until tissue sank, then embedded in OCT (Cat #4583; Sakura Finetek, Torrance, CA). Frozen brain blocks were cut at 20 µm sagittally with a cryostat (Model CM1950; Leica Biosystems, Dear Park, IL). For immunostaining, slides were washed in PBS briefly to remove OCT, then incubated with M.O.M. blocking reagent (Cat #MKB-2213-1; Vector Laboratories, Newark, CA) to block endogenous mouse immunoglobulins. After three washes with PBS, sections were blocked with 10% normal goat serum (Thermo Fisher Scientific) with 0.3% Triton X-100 for 1 h at room temperature. Sections were then incubated overnight at 4°C with primary antibodies anti-SARS-CoV-2 ORF3a (rabbit polyclonal; Cat #PA5-116946; Thermo Fisher Scientific), anti-Strep-tag (mouse monoclonal; Cat#2-1507-001; IBA Lifesciences GmbH, Goettingen, Germany), anti-NeuN (rabbit polyclonal; Cat #ab128886; Abcam, Cambridge, MA), anti-GFAP (rabbit polyclonal; Cat #ab7260; Abcam), anti-Olig2 (rabbit monoclonal; Cat #ab109186; Abcam), anti-Iba1 (rabbit polyclonal; Cat #019-19741; Wako, Richmond, VA), anti-α-synuclein (rabbit polyclonal; Cat #2642S; Cell Signaling Technology, Danvers, MA), anti-NeuN (mouse monoclonal, used in co-staining with α-synuclein; Cat #MAB377; MilliporeSigma, Burlington, MA), or anti-Lamp1 (rat monoclonal; Cat #MABC39; MilliporeSigma), diluted in 2% normal goat serum/PBS. For GM2 ganglioside immunostaining, sections were permeabilized with prechilled acetone for 10 min at -20°C. Sections were air-dried before blocking with M.O.M. blocking reagent, followed by 10% normal goat serum. Sections were incubated for 1 h at room temperature with anti-GM2 ganglioside antibody (mouse monoclonal; Cat #A2576; TCI, Tokyo, Japan) diluted in 2% normal goat serum. After three washes in PBS, sections were incubated for 1 h at room temperature with secondary antibodies Dylight™ 488 goat anti-mouse IgG

(Cat #35503; Thermo Fisher Scientific), Alexa Fluor™ 594 goat anti-mouse IgM (Cat #A-21044; Thermo Fisher Scientific), Alexa Fluor™ 488 goat anti-rabbit (Cat #A-48282; Thermo Fisher Scientific), Dylight™ 594 goat anti-rabbit (Cat #35561; Thermo Fisher Scientific), or Alexa Fluor™ 594 goat anti-rat (Cat #A-11007; Thermo Fisher Scientific), diluted 1:400 in 2% normal goat serum/PBS. Sections were washed and counterstained with DAPI (Thermo Fisher Scientific), then mounted with Prolong Diamond Antifade Mountant (Cat #P36961; Thermo Fisher Scientific). After curing for 24 h, sections were imaged under a Zeiss confocal microscope. For multiple fluorescent staining, images of different channels were analyzed and merged using Fiji/ImageJ to determine relationships between different labels. For fluorescence intensity studies, three to five Z-stacks from each sample were captured under oil objectives of 40× or 63× with the same settings. With 10–15 images/stack, images were measured for fluorescence intensity per pixel using Fiji/ImageJ.⁶⁶

NeuroSilver staining was performed by FD NeuroTechnologies (Columbia, MD) using the FD NeuroSilver™ kit II to detect degenerating neuron in fixed tissue. Sagittal brain sections were cut at 40 µm, stained, and then imaged under a Keyence microscope (Model BZ-X800; Keyence, Itasca, IL). To quantify the silver staining in the regions of interest, 3–5 Z-stacks were captured from each sample under a 40× oil objective using the same settings. With ~10 images/stack, the silver-stained area in the images were measured by thresholding using Fiji/ImageJ.

TUNEL assays were performed using the Click-iT™ plus TUNEL assay kit (Alexa Fluor™ 594 dye; Cat #C10618; Thermo Fisher Scientific) to detect *in situ* apoptotic cells in mouse brain sections. Fresh frozen mouse brains were cut at 20 µm sagittally and fixed in 4% paraformaldehyde for 15 min at room temperature. After washing in PBS, sections were dehydrated with serial gradient ethanol (50%, 70%, 90%, 100%) for 5 min in each concentration. Sections were then air-dried and used for TUNEL labeling following the kit instructions. Sections were counterstained with DAPI and imaged under a Zeiss confocal microscope. For TUNEL-labeled cell counting, stitched images were captured under a 10× objective and quantified using the cell counter function of Fiji/ImageJ.

4.8 | Lipid analyses

Ganglioside analysis of mouse brain was performed by HPTLC. The hemispheres were weighed, and the total lipids were sequentially extracted by 1:1 (v/v) and

1:2 (v/v) of chloroform-methanol (C-M), and 30:60:8 (v/v/v) of chloroform-methanol-water (C-M-W). The lipid extract was dried under nitrogen gas and separated to polar (upper) and nonpolar (lower) phases by Folch's method.⁶⁷ To enrich gangliosides, mild alkaline treatment of the upper phase was performed by evaporating the organic solvent in the upper phase and incubating it in 0.1 N NaOH at 40°C for 2 h. The solution was neutralized by acetic acid, diluted twice with 0.1 M KCl, and desalinated using a Sep-Pak C18 column (Part # WAT020805; Waters, Milford, MA). Prior to sample application, the Sep-Pak C18 column was washed with three column volumes, five column volumes methanol and water and two column volumes of 0.1 M KCl. After sample application, the salt was washed out by five column volumes of water and the gangliosides were eluted by 2 mL of methanol and 6 mL of 1:1 (v/v) of C-M. The eluate was dried, dissolved in 200 μL of 30:60:8 (v/v/v) of C-M-W, and an aliquot (10 μL, gangliosides from approximately 12.5 mg brain tissue) applied to HPTLC and developed in 55:45:10 (v/v/v) of C-M-0.2% CaCl₂. The HPTLC plate was dried and sprayed with resorcinol reagent, tightly covered with a glass plate using clips, and positioned facing down in a 90°C oven for 15 min. The gangliosides were visualized as blue-violet bands. The R_f values of standards (Cat #1065&1508; Matraya LLC, State College, PA), applied on the same HPTLC plate, were compared with bands in the samples. Resorcinol reagent was prepared by adding 80 mL of concentrated HCl and 0.25 mL of 0.1 M CuSO₄ to aqueous resorcinol solution (200 mg resorcinol (Cat # R1000; Sigma-Aldrich, St. Louis, MO) in 10 mL of water) and adjusting the final volume to 100 mL using water. The HPTLC plate was imaged on the Amersham Imager 680 (GE Healthcare Life Sciences, Marlborough, MA). The ganglioside bands of each sample were quantified using Fiji/ImageJ.⁶⁸

Hexosylceramides in HeLa cell lines were measured by HPLC-tandem mass spectrometry by the Lipidomics Core at the Medical University of South Carolina as described.⁶⁸

4.9 | Western blotting

Mouse brain hemispheres, kidney, lung, or liver was homogenized in RIPA Lysis and Extraction buffer (Thermo Fisher Scientific) supplemented with 1% SDS, HALT protease inhibitor cocktail (Thermo Fisher Scientific), and HALT phosphatase inhibitor cocktail (Thermo Fisher Scientific). Equal amounts of lysed protein samples (30 μg) were separated on either a NuPAGE 4–12% Bis-Tris gel or 12% Bis-Tris gel (Thermo Fisher

Scientific) under denaturing conditions and transferred onto a nitrocellulose membrane using the iBlot2 Blotting System (Thermo Fisher Scientific). The membranes were blocked in 5% nonfat dry milk for 1 h at room temperature and incubated overnight at 4°C with primary antibodies for SARS-CoV-2 ORF3a (Thermo Fisher Scientific), p62/SQSTM1 (Cat#P0067; MilliporeSigma), or LAMP1 (Abcam). Membranes were then washed in 5% nonfat dry milk and incubated with goat anti-rabbit IgG horseradish peroxidase-conjugated secondary antibody (Cat#AP132P; MilliporeSigma) for 1 h at room temperature in 5% nonfat dry milk. Membranes were developed using the ECL prime Western blotting system (Cat#GERPN2232; MilliporeSigma) and imaged on the Amersham Imager 680. A β-actin antibody (Cat#ab49900; Abcam) was used as a loading control for all membranes. Blot signals were quantified using Fiji/ImageJ.⁶⁶

4.10 | Statistical analysis

Comparisons were analyzed for statistical significance using unpaired *t* tests (one analyte) or multiple unpaired *t* tests (multiple analytes) between ORF3a and control groups to determine the *p*-value using Prism software (GraphPad Software, Inc.). All the results were presented as mean ± SD. A value of *p* < .05 was considered significant.

4.11 | Study approval

All mouse studies were approved by the National Institute of Diabetes and Digestive and Kidney Diseases Animal Care and Use Committee.

AUTHOR CONTRIBUTIONS

Hongling Zhu and Richard L. Proia designed the study. Hongling Zhu, Colleen Byrnes, Y. Terry Lee, Galina Tumetova, Hannah B. D. Duffy, Sydney N. Pettit, Jenna Y. Bakir, Jabili Angina, Danielle A. Springer, Maria L. Allende, and Mari Kono conducted the experiments. Hongling Zhu and Richard L. Proia wrote the original draft of the manuscript. Hongling Zhu, Colleen Byrnes, Y. Terry Lee, Galina Tumetova, Hannah B. D. Duffy, Sydney N. Pettit, Jenna Y. Bakir, Danielle A. Springer, Maria L. Allende, Mari Kono, and Richard L. Proia reviewed and edited the manuscript.

ACKNOWLEDGMENTS

This work was supported by the Intramural Research Programs of the National Institutes of Health, the National Institute of Diabetes and Digestive and Kidney Diseases, and the National Heart, Lung, and Blood Institute and

in part by the Lipidomics Shared Resource, Hollings Cancer Center, Medical University of South Carolina (P30 CA138313 and P30 GM103339). Graphical illustrations were created with [BioRender.com](https://biorender.com). The content is solely the responsibility of the authors and does not necessarily represent the official views of the National Institutes of Health.

DISCLOSURES

The authors have declared that no conflict of interest exists.

DATA AVAILABILITY STATEMENT

The RNA-Seq data discussed in this publication have been deposited in NCBI's Gene Expression Omnibus⁶⁹ and are accessible through GEO Series accession number GSE224290. All other data generated or analyzed during this study are included in this manuscript and supplementary information files.

ORCID

Hongling Zhu  <https://orcid.org/0000-0003-0612-009X>

Hannah B. D. Duffy  <https://orcid.org/0000-0002-0358-6997>

Jenna Y. Bakir  <https://orcid.org/0000-0003-4314-9115>

Sydney N. Pettit  <https://orcid.org/0009-0002-3720-6144>

Maria L. Allende  <https://orcid.org/0000-0001-9930-8563>

Mari Kono  <https://orcid.org/0000-0003-2447-4350>

Richard L. Proia  <https://orcid.org/0000-0003-0456-1270>

REFERENCES

- Spudich S, Nath A. Nervous system consequences of COVID-19. *Science*. 2022;375(6578):267-269.
- Gupta A, Madhavan MV, Sehgal K, et al. Extrapulmonary manifestations of COVID-19. *Nat Med*. 2020;26(7):1017-1032.
- Iadecola C, Anrather J, Kamel H. Effects of COVID-19 on the nervous system. *Cell*. 2020;183(1):16-27 e1.
- Monje M, Iwasaki A. The neurobiology of long COVID. *Neuron*. 2022;110(21):3484-3496.
- Reiken S, Dridi H, Sittenfeld L, Liu X, Marks AR. Alzheimer's-like remodeling of neuronal ryanodine receptor in COVID-19. *bioRxiv* 2021.
- Wang L, Davis PB, Volkow ND, Berger NA, Kaelber DC, Xu R. Association of COVID-19 with new-onset Alzheimer's disease. *J Alzheimers Dis*. 2022;89(2):411-414.
- Matschke J, Lutgehetmann M, Hagel C, et al. Neuropathology of patients with COVID-19 in Germany: a post-mortem case series. *Lancet Neurol*. 2020;19(11):919-929.
- Yang AC, Kern F, Losada PM, et al. Dysregulation of brain and choroid plexus cell types in severe COVID-19. *Nature*. 2021;595(7868):565-571.
- Song E, Zhang C, Israelow B, et al. Neuroinvasion of SARS-CoV-2 in human and mouse brain. *J Exp Med*. 2021;218(3):e20202135.
- Crunfli F, Carregari VC, Veras FP, et al. Morphological, cellular, and molecular basis of brain infection in COVID-19 patients. *Proc Natl Acad Sci USA*. 2022;119(35):e2200960119.
- Rutkai I, Mayer MG, Hellmers LM, et al. Neuropathology and virus in brain of SARS-CoV-2 infected non-human primates. *Nat Commun*. 2022;13(1):1745.
- Beckman D, Bonillas A, Diniz GB, et al. SARS-CoV-2 infects neurons and induces neuroinflammation in a non-human primate model of COVID-19. *Cell Rep*. 2022;41:111573.
- Meinhardt J, Radke J, Dittmayer C, et al. Olfactory transmucosal SARS-CoV-2 invasion as a port of central nervous system entry in individuals with COVID-19. *Nat Neurosci*. 2021;24(2):168-175.
- Ramani A, Muller L, Ostermann PN, et al. SARS-CoV-2 targets neurons of 3D human brain organoids. *EMBO J*. 2020;39(20):e106230.
- Andrews MG, Mukhtar T, Eze UC, et al. Tropism of SARS-CoV-2 for human cortical astrocytes. *Proc Natl Acad Sci USA*. 2022;119(30):e2122236119.
- Kern DM, Sorum B, Mali SS, et al. Cryo-EM structure of SARS-CoV-2 ORF3a in lipid nanodiscs. *Nat Struct Mol Biol*. 2021;28(7):573-582.
- Zhang J, Ejikemeuwa A, Gerzanich V, et al. Understanding the role of SARS-CoV-2 ORF3a in viral pathogenesis and COVID-19. *Front Microbiol*. 2022;13:854567.
- McGrath ME, Xue Y, Dillen C, et al. SARS-CoV-2 variant spike and accessory gene mutations alter pathogenesis. *Proc Natl Acad Sci USA*. 2022;119(37):e2204717119.
- Chen D, Zheng Q, Sun L, et al. ORF3a of SARS-CoV-2 promotes lysosomal exocytosis-mediated viral egress. *Dev Cell*. 2021;56(23):3250-63 e5.
- Miao G, Zhao H, Li Y, et al. ORF3a of the COVID-19 virus SARS-CoV-2 blocks HOPS complex-mediated assembly of the SNARE complex required for autolysosome formation. *Dev Cell*. 2021;56(4):427-42 e5.
- Ren Y, Shu T, Wu D, et al. The ORF3a protein of SARS-CoV-2 induces apoptosis in cells. *Cell Mol Immunol*. 2020;17(8):881-883.
- Zhang J, Li Q, Cruz Cosme RS, et al. Genome-wide characterization of SARS-CoV-2 cytopathogenic proteins in the search of antiviral targets. *mBio*. 2021;13(1):e0016922.
- Siu KL, Yuen KS, Castano-Rodriguez C, et al. Severe acute respiratory syndrome coronavirus ORF3a protein activates the NLRP3 inflammasome by promoting TRAF3-dependent ubiquitination of ASC. *FASEB J*. 2019;33(8):8865-8877.
- Walkley SU. Secondary accumulation of gangliosides in lysosomal storage disorders. *Semin Cell Dev Biol*. 2004;15(4):433-444.
- Nixon RA. The role of autophagy in neurodegenerative disease. *Nat Med*. 2013;19(8):983-997.
- Boland S, Swarup S, Ambaw YA, et al. Deficiency of the frontotemporal dementia gene GRN results in gangliosidosis. *Nat Commun*. 2022;13(1):5924.
- Goedert M. Alpha-synuclein and neurodegenerative diseases. *Nat Rev Neurosci*. 2001;2(7):492-501.
- Mathiesen SN, Lock JL, Schoderboeck L, Abraham WC, Hughes SM. CNS transduction benefits of AAV-PHP.eB over AAV9 are dependent on administration route and mouse strain. *Mol Ther Methods Clin Dev*. 2020;19:447-458.
- Chan KY, Jang MJ, Yoo BB, et al. Engineered AAVs for efficient noninvasive gene delivery to the central and peripheral nervous systems. *Nat Neurosci*. 2017;20(8):1172-1179.

30. Gong Y, Qin S, Dai L, Tian Z. The glycosylation in SARS-CoV-2 and its receptor ACE2. *Signal Transduct Target Ther.* 2021;6(1):396.
31. Gallyas F. Chemical nature of the first products (nuclei) of the argyrophil staining. *Acta Histochem.* 1980;67(2):145-158.
32. Gavrieli Y, Sherman Y, Ben-Sasson SA. Identification of programmed cell death in situ via specific labeling of nuclear DNA fragmentation. *J Cell Biol.* 1992;119(3):493-501.
33. Vanderheiden A, Klein RS. Neuroinflammation and COVID-19. *Curr Opin Neurobiol.* 2022;76:102608.
34. Savelieff MG, Feldman EL, Stino AM. Neurological sequela and disruption of neuron-glia homeostasis in SARS-CoV-2 infection. *Neurobiol Dis.* 2022;168:105715.
35. Streit WJ, Xue QS, Tischer J, Bechmann I. Microglial pathology. *Acta Neuropathol Commun.* 2014;2:142.
36. Arshad N, Laurent-Rolle M, Ahmed WS, et al. SARS-CoV-2 accessory proteins ORF7a and ORF3a use distinct mechanisms to downregulate MHC-I surface expression. *bioRxiv* 2022.
37. Bodro M, Compta Y, Llanso L, et al. Increased CSF levels of IL-1beta, IL-6, and ACE in SARS-CoV-2-associated encephalitis. *Neurol Neuroimmunol Neuroinflamm.* 2020;7(5):e821.
38. Mizushima N, Yamamoto A, Matsui M, Yoshimori T, Ohsumi Y. In vivo analysis of autophagy in response to nutrient starvation using transgenic mice expressing a fluorescent autophagosome marker. *Mol Biol Cell.* 2004;15(3):1101-1111.
39. Bjorkoy G, Lamark T, Pankiv S, Overvatn A, Brech A, Johansen T. Monitoring autophagic degradation of p62/SQSTM1. *Methods Enzymol.* 2009;452:181-197.
40. Webb JL, Ravikumar B, Atkins J, Skepper JN, Rubinsztein DC. Alpha-synuclein is degraded by both autophagy and the proteasome. *J Biol Chem.* 2003;278(27):25009-25013.
41. Cheng XT, Xie YX, Zhou B, Huang N, Farfel-Becker T, Sheng ZH. Characterization of LAMP1-labeled nondegradative lysosomal and endocytic compartments in neurons. *J Cell Biol.* 2018;217(9):3127-3139.
42. Chen CS, Patterson MC, Wheatley CL, O'Brien JF, Pagano RE. Broad screening test for sphingolipid-storage diseases. *Lancet.* 1999;354(9182):901-905.
43. Pagano RE, Puri V, Dominguez M, Marks DL. Membrane traffic in sphingolipid storage diseases. *Traffic.* 2000;1(11):807-815.
44. Sillence DJ, Puri V, Marks DL, et al. Glucosylceramide modulates membrane traffic along the endocytic pathway. *J Lipid Res.* 2002;43(11):1837-1845.
45. te Vruchte D, Speak AO, Wallom KL, et al. Relative acidic compartment volume as a lysosomal storage disorder-associated biomarker. *J Clin Invest.* 2014;124(3):1320-1328.
46. Nixon RA. The aging lysosome: an essential catalyst for late-onset neurodegenerative diseases. *Biochim Biophys Acta Proteins Proteom.* 2020;1868(9):140443.
47. Yang S, Tian M, Johnson AN. SARS-CoV-2 protein ORF3a is pathogenic in *Drosophila* and causes phenotypes associated with COVID-19 post-viral syndrome. *bioRxiv* 2020. [10.1101/2020.12.20.423533](https://doi.org/10.1101/2020.12.20.423533)
48. Xu H, Akinyemi IA, Chitre SA, et al. SARS-CoV-2 viroporin encoded by ORF3a triggers the NLRP3 inflammatory pathway. *Virology.* 2022;568:13-22.
49. Cooper O, Hallett P, Isacson O. Upstream lipid and metabolic systems are potential causes of Alzheimer's disease, Parkinson's disease and dementias. *FEBS J.* 2022. doi:[10.1111/febs.16638](https://doi.org/10.1111/febs.16638)
50. van Echten-Deckert G, Walter J. Sphingolipids: critical players in Alzheimer's disease. *Prog Lipid Res.* 2012;51(4):378-393.
51. Wang G, Bieberich E. Sphingolipids in neurodegeneration (with focus on ceramide and S1P). *Adv Biol Regul.* 2018;70:51-64.
52. Rhodes CH, Priemer DS, Karlovich E, Perl DP, Goldman J. B-Amyloid deposits in young COVID patients. *SSRN*; 2022. doi:[10.2139/ssrn.4003213](https://doi.org/10.2139/ssrn.4003213)
53. Philippens I, Boszormenyi KP, Wubben JAM, et al. Brain inflammation and intracellular alpha-synuclein aggregates in macaques after SARS-CoV-2 infection. *Viruses.* 2022;14(4). doi:[10.3390/v14040776](https://doi.org/10.3390/v14040776)
54. Kaufer C, Schreiber CS, Hartke AS, et al. Microgliosis and neuronal proteinopathy in brain persist beyond viral clearance in SARS-CoV-2 hamster model. *EBioMedicine.* 2022;79:103999.
55. Vitner EB, Avraham R, Politi B, Melamed S, Israely T. Elevation in sphingolipid upon SARS-CoV-2 infection: possible implications for COVID-19 pathology. *Life Sci Alliance.* 2022;5(1):e202101168.
56. Kanou S, Wardeh L, Govindarajan S, Macnay K. Guillain-Barre syndrome (GBS) associated with COVID-19 infection that resolved without treatment in a child. *BMJ Case Rep.* 2022;15:e245455.
57. Abu-Rumeileh S, Abdelhak A, Foschi M, Tumani H, Otto M. Guillain-Barre syndrome spectrum associated with COVID-19: an up-to-date systematic review of 73 cases. *J Neurol.* 2021;268(4):1133-1170.
58. Dufour C, Co TK, Liu A. GM1 ganglioside antibody and COVID-19 related Guillain Barre syndrome—a case report, systemic review and implication for vaccine development. *Brain Behav Immun Health.* 2021;12:100203.
59. Nguyen L, McCord KA, Bui DT, et al. Sialic acid-containing glycolipids mediate binding and viral entry of SARS-CoV-2. *Nat Chem Biol.* 2022;18(1):81-90.
60. Gordon DE, Jang GM, Bouhaddou M, et al. A SARS-CoV-2 protein interaction map reveals targets for drug repurposing. *Nature.* 2020;583(7816):459-468.
61. Jeyakumar M, Butters TD, Cortina-Borja M, et al. Delayed symptom onset and increased life expectancy in Sandhoff disease mice treated with N-butyldeoxojirimycin. *Proc Natl Acad Sci USA.* 1999;96(11):6388-6393.
62. Guyenet SJ, Furrer SA, Damian VM, Baughan TD, La Spada AR, Garden GA. A simple composite phenotype scoring system for evaluating mouse models of cerebellar ataxia. *J Vis Exp.* 2010;39:e1787. doi:[10.3791/1787](https://doi.org/10.3791/1787)
63. Liao Y, Smyth GK, Shi W. featureCounts: an efficient general purpose program for assigning sequence reads to genomic features. *Bioinformatics.* 2014;30(7):923-930.
64. Love MI, Huber W, Anders S. Moderated estimation of fold change and dispersion for RNA-seq data with DESeq2. *Genome Biol.* 2014;15(12):550.
65. Yu G, Wang LG, Han Y, He QY. clusterProfiler: an R package for comparing biological themes among gene clusters. *Omics.* 2012;16(5):284-287.
66. Schneider CA, Rasband WS, Eliceiri KW. NIH image to ImageJ: 25 years of image analysis. *Nat Methods.* 2012;9(7):671-675.
67. Folch J, Lees M, Sloane Stanley GH. A simple method for the isolation and purification of total lipides from animal tissues. *J Biol Chem.* 1957;226(1):497-509.
68. Bielawski J, Pierce JS, Snider J, Rembiesa B, Szulc ZM, Bielawska A. Comprehensive quantitative analysis of bioactive sphingolipids by high-performance liquid chromatography-tandem mass spectrometry. *Methods Mol Biol.* 2009;579:443-467.

69. Edgar R, Domrachev M, Lash AE. Gene expression omnibus: NCBI gene expression and hybridization array data repository. *Nucleic Acids Res.* 2002;30(1):207-210.

SUPPORTING INFORMATION

Additional supporting information can be found online in the Supporting Information section at the end of this article.

How to cite this article: Zhu H, Byrnes C, Lee YT, et al. SARS-CoV-2 ORF3a expression in brain disrupts the autophagy-lysosomal pathway, impairs sphingolipid homeostasis, and drives neuropathogenesis. *The FASEB Journal*. 2023;37:e22919. doi:[10.1096/fj.202300149R](https://doi.org/10.1096/fj.202300149R)